

Vertical fracture detection by exploiting the polarization properties of ground-penetrating radar signals

Georgios P. Tsoflias*, Jean-Paul Van Gestel[†], Paul L. Stoffa**, Donald D. Blankenship[§], and Mrinal Sen[§]

ABSTRACT

Vertically oriented thin fractures are not always detected by conventional single-polarization reflection profiling ground-penetrating radar (GPR) techniques. We study the polarization properties of EM wavefields and suggest multipolarization acquisition surveying to detect the location and azimuth of vertically oriented fractures. We employ analytical solutions, 3D finite-difference time-domain modeling, and field measurements of multipolarization GPR data to investigate EM wave transmission through fractured geologic formations. For surface-based multipolarization GPR measurements across vertical fractures, we observe a phase lead when the incident electric-field component is oriented perpendicular to the plane of the fracture. This observation is consistent for nonmagnetic geologic environments and allows the determination of vertical fracture location and azimuth based on the presence of a phase difference and a phase lead relationship between varying polarization GPR data.

INTRODUCTION

Ground-penetrating radar (GPR) reflection surveying of single-offset, copolarized data provides high-resolution profiles of geologic formations (Davis and Annan, 1989). Multi-offset GPR surveys (Fisher et al., 1992), 3D surveys (Grasmueck, 1996; McMechan et al., 1997; Tsoflias and Sharp, 1998), and time-lapse techniques (Brewster and Annan, 1994; Birken and Versteeg, 1998), analogous to seismic data techniques, have also been used successfully to characterize the near surface. These GPR reflection surveys routinely image subhorizontal

fractures at or near normal incidence (Tsoflias et al., 2001). Vertical fracture zones, although not directly imaged by conventional surface reflection GPR data, can be inferred when significant vertical displacement of horizontal strata has occurred along the plane of the fracture (Grasmueck, 1996). Thin fractures in aquifers and reservoirs are commonly near vertical and do not offset bedding planes beyond the vertical resolution limits of typical GPR surveys (a few centimeters to meters). Thus, constant polarization reflection data offer very limited information about the presence of thin (relative to wavelength $< \lambda/50$), vertically oriented fractures. Fractures are important in determining reservoir fluid flow properties and, when vertically oriented, provide the conduits for aquifer recharge and/or rapid infiltration of contaminants.

Limited published work has investigated GPR signal polarization effects on geologic formations and the detection of fractures. Coon et al. (1981), while investigating the feasibility of short-pulse radar surveying in coal seams, observe that EM energy polarized perpendicular to bedding planes of the seam propagates to greater distances than when polarized parallel to the seams. Kovacs and Morey (1978) field experiments show radar amplitude variations as a function of electric-field orientation and ice crystal *c*-axis orientation. Tillard (1994) further observes propagation velocity variations as a function of relative permittivity anisotropy in schists. Miwa et al. (1999) develop a polarimetric borehole radar and use it to analyze reflections from subsurface fractures. Lehman et al. (2000) present the advantages of using multicomponent GPR for improved subsurface reflection imaging. Van Gestel and Stoffa (2001) use Alford rotation (Alford, 1986) to extract the main axis of subsurface anisotropy and the orientation of buried objects from multipolarization GPR data.

In this study we investigate the polarization properties of EM wavefields to detect vertical fractures and use multipolarization

Manuscript received by the Editor January 7, 2002; revised manuscript received November 24, 2003.

*Formerly University of Texas at Austin, Department of Geological Sciences and Institute for Geophysics, Austin, Texas 78759; presently The University of Kansas, Lawrence, Kansas 66045. E-mail: tsoflias@ku.edu.

[†]Formerly University of Texas at Austin, Department of Geological Sciences and Institute for Geophysics, Austin, Texas, 78759; presently BP, Houston, Texas 77079. E-mail: jeanpaul@vangestel.com.

**University of Texas at Austin, Department of Geological Sciences and Institute for Geophysics, Austin, Texas 78759. E-mail: pauls@ig.utexas.edu.

[§]University of Texas at Austin, Institute for Geophysics, Austin, Texas 78759. E-mail: blank@ig.utexas.edu; mrinal@ig.utexas.edu.

© 2004 Society of Exploration Geophysicists. All rights reserved.

acquisition of GPR data to determine the location and azimuth of vertically oriented fractures. We evaluate EM wave transmission through a fractured formation by using analytical solutions, 3D finite-difference time-domain simulations, and field measurements of multipolarization GPR data. Our study shows that at large oblique angles of incidence to the fracture, when the electric field component is oriented perpendicular to the plane of the fracture (referred to as H -pol), the transmitted through-the-fracture electric field leads in phase compared to when the incident electric field is oriented parallel to the plane of the fracture (referred to as E -pol). This observation is consistent for nonmagnetic geologic environments and allows for the determination of vertical fracture location and azimuth based on the presence of a phase lead in H -pol data relative to E -pol data.

ANALYTIC SOLUTIONS AND APPLICATION TO GEOLOGIC MATERIALS

Methods

Plane-wave oblique incidence reflection and transmission at planar layered media are presented in EM field theory texts (Stratton, 1941; Balanis, 1989; Chew, 1990). In the simplified case shown in Figure 1, Snell's law of reflection and refraction, which is independent of polarization, defines the same travel-path for both H -pol and E -pol waves. The EM wave impinges at low incident angles to horizontal bedding planes (θ_{ib} measured from vertical) and at high incident angles to the vertical

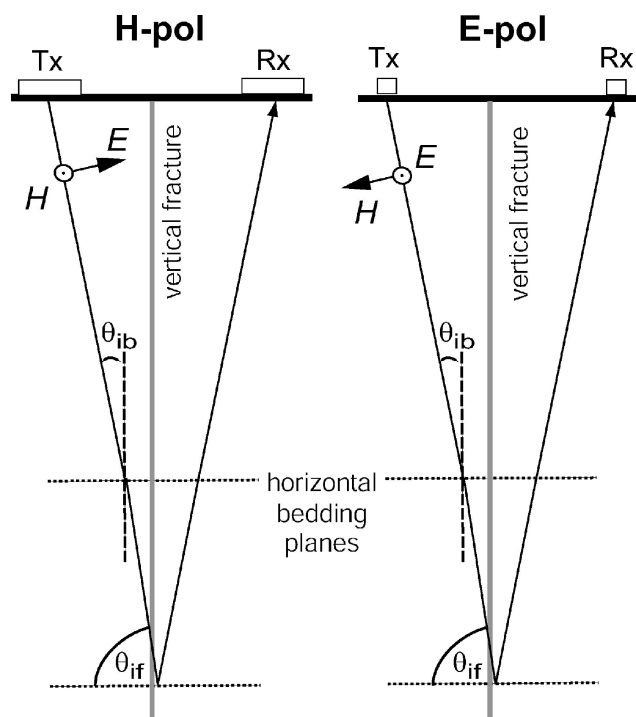


Figure 1. Cross-section of dual polarization wavefield geometry. H -pol: transmitter (Tx), receiver (Rx) dipole antennas, and electric field (\mathbf{E}) oriented perpendicular to the plane of the fracture. E -pol: Tx, Rx, and \mathbf{E} oriented parallel to the plane of the fracture. \mathbf{H} is the magnetic field, θ_{if} is the angle of incidence to the fracture plane, and θ_{ib} is the angle of incidence to the bedding plane.

fracture (θ_{if} measured from horizontal). At dielectric interfaces, the complex transmission (and reflection) coefficients are a function of the polarization of the incident wavefields and result in differences in amplitude and phase between the transmitted (and reflected) H -pol and E -pol waves.

We determine analytically H -pol and E -pol net transmission coefficients (T_H and T_E , respectively) through a three-layer case (1–rock matrix; 2–fracture; 3–rock matrix) as the ratio of the transmitted electric field in medium 3 to the incident electric field in medium 1. Electric and magnetic fields are computed by the recursive method employed in EM plane-wave studies, which considers field continuity and matching of the impedances across boundaries (Balanis, 1989; Cardwell, written communication, 1997). We evaluate T_H and T_E at varying angles of incidence for nonmagnetic, lossy, unsaturated and water-saturated geologic environments of low dielectric constant (ϵ_r), such as granite, sand, and dolomite, as well as high dielectric constant environments, such as shale, silt, and clays. The fracture (layer 2) is assumed to be filled with air, fresh water, or sea water, ranging in aperture from 0.5 m (approximately one wavelength λ in the rock matrix for a 200-MHz signal) to 1 mm ($\sim\lambda/500$). Selected T_H and T_E computations are demonstrated graphically in Figure 2.

Results

Figure 2 shows the complex T_H and T_E magnitude, phase, and phase difference $\Delta\phi$ of a 200-MHz signal evaluated for a range of angles of incidence θ_{if} for dolomite ($\epsilon_r = 8$, $\sigma = 0.2$ mS/m, $\lambda \cong 50$ cm) containing a 1-cm-aperture water-saturated fracture ($\epsilon_r = 80$, $\sigma = 46.5$ mS/m) and for silt ($\epsilon_r = 30$, $\sigma = 100$ mS/m, $\lambda \cong 35$ cm) containing a 1-cm-aperture dry fracture ($\epsilon_r = 1$,

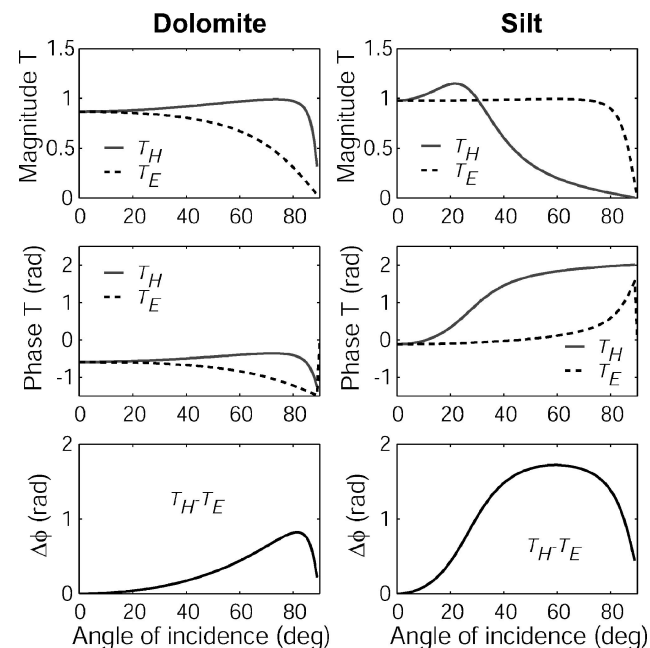


Figure 2. Analytical solutions of the magnitude, phase, and phase difference ($\Delta\phi$) of net H -pol transmission coefficient (T_H) and E -pol transmission coefficient (T_E) at 200 MHz frequency for low ϵ_r and σ dolomite rock matrix containing a 1-cm water-saturated fracture and high ϵ_r and σ silt rock matrix containing a 1-cm air-filled fracture.

$\sigma = 0$ mS/m). Analytical solutions of the models indicate the following

- 1) the $\Delta\phi$ between T_H and T_E shows a consistent phase lead of T_H at oblique angles of incidence;
- 2) $\Delta\phi$ is zero at low angles of incidence and increases as the angle of incidence increases;
- 3) T_H and T_E magnitudes are equal at low angles of incidence, and;
- 4) T_H and T_E magnitudes do not display a consistent trend with increasing angle of incidence.

The transmission coefficient (and consequently the reflection coefficient) phase difference between the two polarizations ($\Delta\phi$) vanishes for small angles of incidence (normal and near-normal incidence, $\theta \cong 0^\circ$). For the acquisition geometry depicted in Figure 1, small transmitter–receiver (Tx–Rx) offset would result in near-normal incidence ($\theta_{ib} \cong 0^\circ$) to horizontal bedding planes in the subsurface; thus, no phase difference between T_H and T_E would be introduced by transmission and reflection at the horizontal bedding plane interfaces. However, small Tx–Rx offset would result in large angles of incidence (θ_{if}) to the vertical plane of the fracture and would yield $\Delta\phi$. Thus, small-offset H -pol and E -pol data acquired in the simplified setting of Figure 1 would be expected to show a phase difference as a result of the presence of the vertical fracture. Furthermore, $\Delta\phi$ would be expected to increase with increasing depth because the angle of incidence to the vertical fracture plane θ_{if} would increase.

3D NUMERICAL MODELING

Methods

We use a modified 3D, three-component, finite-difference time-domain modeling code (Roberts, 1994; Roberts and Daniels, 1997) to study the transmission of the EM wavefields through geologic layered media. The 3D finite-difference time-domain model enabled the study of both E -pol and H -pol transmission through a thin layer in an otherwise homogeneous medium. Although planar layered surfaces in homogeneous media are not an accurate representation of naturally occurring fractures, such a model gives useful insight and support to this study.

We set the modeling parameters to represent a fractured dolomite environment with EM characteristics similar to those at the Bissen Quarry field site investigated. Dolomite matrix and groundwater electrical conductivity σ values for the field site are from Muldoon and Bradbury (1996). Dolomite parameters are $\sigma = 0.22$ mS/m and $\epsilon_r = 8$. The dolomite is non-magnetic, and the fracture is considered air filled ($\sigma = 0$ mS/m, $\epsilon_r = 1$) and freshwater saturated ($\sigma = 45.6$ mS/m, $\epsilon_r = 80$). The fracture is modeled using a 1-cm grid size in three dimensions, 0.0175-ns time step, 200-MHz source center frequency, and fracture aperture of 1 gridpoint (1 cm).

Results

Figure 3 shows the observed 3D finite-difference time-domain E -pol and H -pol electric fields for a 200-MHz transmitted EM wavefield in dolomite across the plane of a vertical, 1-cm aperture, air-filled fracture at 0° , 45° , and 80° angles

of incidence from horizontal. At oblique angles of incidence, the fracture (aperture $d \approx \lambda$ matrix/50) introduces a phase difference (apparent time difference) between H -pol and E -pol transmitted fields, with the H -pol field consistently leading the E -pol field. Normal incidence to the fracture plane (Figure 3a) indicates no phase difference, whereas increasing angles of incidence (Figures 3b,c) show increasing phase lead (apparent time lead) of the H -pol. Figure 4 displays 3D finite-difference time-domain results for the same dolomite model used to generate Figure 3c, but with a freshwater-filled fracture. The H -pol again leads E -pol and displays decreased phase difference compared with the dry fracture model (Figure 3c). In addition, significant amplitude differences and waveform stretching effects are observed in the modeled data in Figures 3c and 4. The amplitude changes once again do not yield consistent trends between varying polarizations.

Additional 3D finite-difference time-domain simulations of H -pol and E -pol wavefields propagating across and along the plane of a vertical fracture in varying rock types consistently show H -pol leading in-phase E -pol. These observations are consistent with the results expected from the analytic solutions. In the following analysis of multipolarization field data, we investigate waveform time differences between corresponding varying polarization data and examine their relationships to vertical fractures.

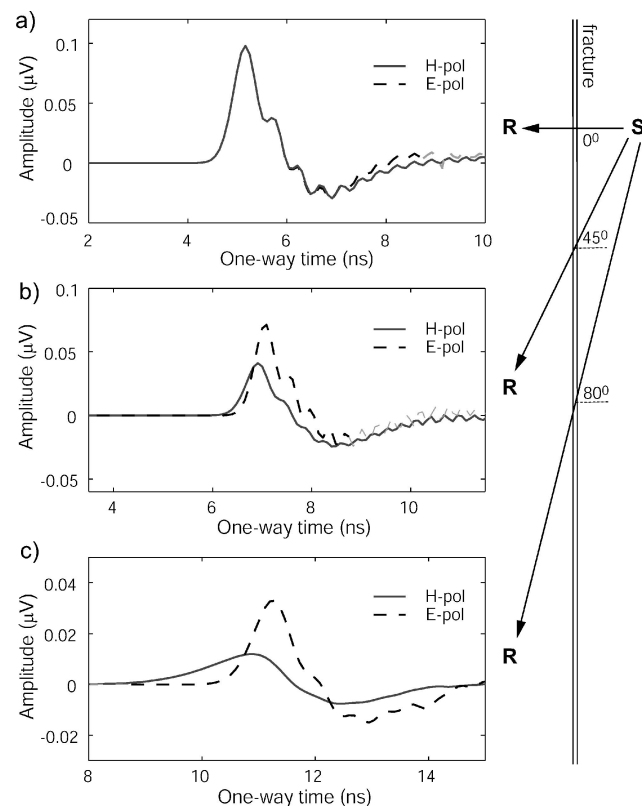


Figure 3. The 200-MHz H -pol and E -pol 3D finite-difference time-domain generated wavefields at source location S and observed at receiver location R for a dolomite matrix containing a 1-cm air-filled fracture. (a) Transmission at normal incidence to the plane of the fracture, (b) 45° angle of incidence, and (c) 80° angle of incidence.

FIELD OBSERVATIONS

Methods

We collected multipolarization surface reflection GPR data at Bissen Quarry, 7.5 km southwest of Sturgeon Bay in Door County, Wisconsin. The site is approximately 40 × 25 m of exposed Silurian Byron Dolomite with visible vertical fractures. Recharge occurs through vertical fractures, and lateral rapid flow occurs through regional horizontal high-permeability zones. The hydrogeologic properties of the site are presented in Muldoon et al. (2001). The water table was at 2 m depth (~38 ns two-way time) during data collection. We used the Pulse EKKO 100 system by Sensors & Software at 200 MHz center frequency, with the surface dipole antennas at 1.5-m, 1-m, and 0.5-m offsets and at varying polarization configurations. Good-quality data were recorded to a depth of approximately 12 m (240 ns two-way time). Vertical fracture surface traces could be clearly seen on the quarry floor; fracture apertures ranged from 2 cm to closed, backfilled with dolomite fragments and soil (Figure 5). Hydraulic tests at this site have indicated vertical flow and communication between fractures (Muldoon and Bradbury, 1998). Thus, we expect vertical fractures to extend several meters below surface, but perhaps not as continuous planar surfaces.

Single midpoint data.—We collected multipolarization surface reflection data at selected locations on the quarry floor where fracture traces were clearly visible and at one location where no fracture trace was visible at the surface. For each location (midpoint) *E*-pol, *H*-pol, and oblique polarization (45° and 135°) data were acquired relative to the surface trace of the vertical fracture (Figure 6). The dipole antennas generate a linearly polarized electric field oriented along the long axis of the antenna. Configurations A and B (Figure 6) maintained a constant Tx–Rx orientation relative to each other (A: broad-fire, i.e., antennas parallel to each other; B: endfire, i.e., antennas along line) and altered the wavefield propagation azimuth to change the electric-field orientation relative to the fracture plane. Configurations C and D maintained the wavefield propagation azimuth constant (i.e., identical travelpaths) and altered the orientation of the electric field by rotating the antennas in place. Antenna configuration C corresponds to the

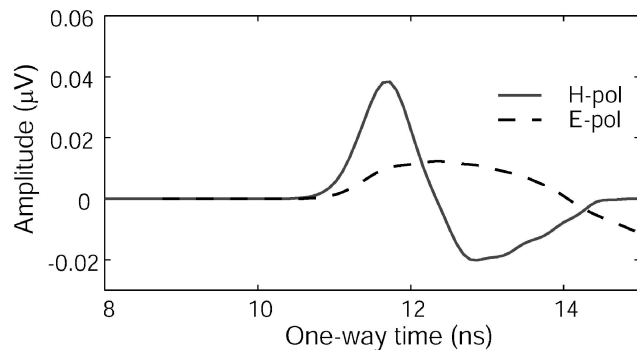


Figure 4. The 200-MHz *H*-pol and *E*-pol 3D finite-difference time-domain generated wavefields transmitted through a fractured dolomite with a 1-cm freshwater-filled fracture at 80° angle of incidence.

cross-section of Figure 1 and the modeled data presented in Figures 3 and 4.

Multipolarization 2D survey line.—We also acquired a fourfold multipolarization 2D line (also referred to as a

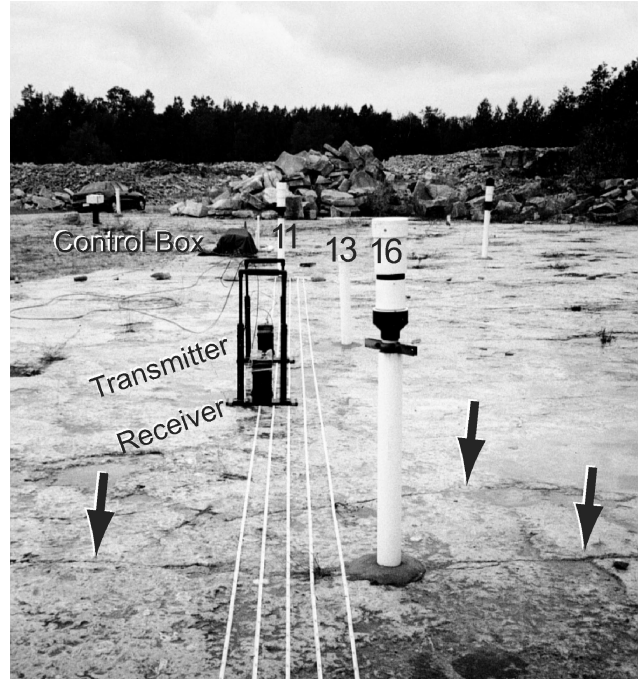


Figure 5. Bissen Quarry field site photograph showing the Pulse EKKO 100 GPR system along with wells 16, 13, and 11. Arrows point to vertical fracture traces on the quarry floor.

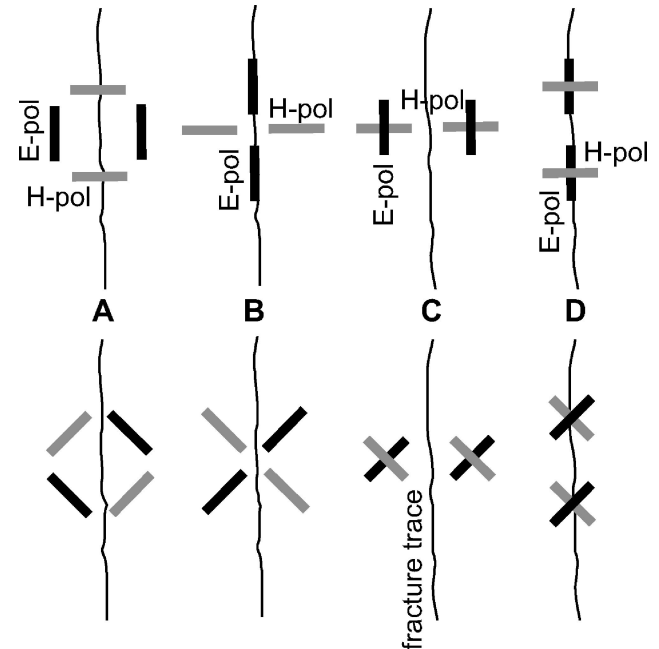


Figure 6. Top view of a fracture trace along the quarry floor and the four dipole antenna configurations used to collect multipolarization data (refer to text for description). Corresponding antenna pairs are identified by grayscale shading.

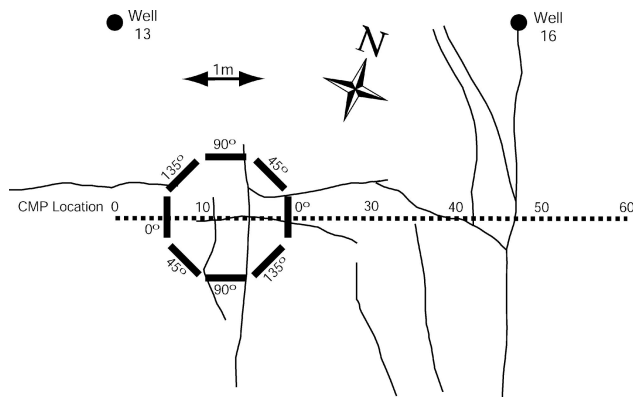


Figure 7. Top view of the fourfold 2D multi-azimuth survey line geometry drawn to scale. Antenna positions are shown for midpoint 13, and corresponding antenna pairs are identified by azimuth relative to the survey line. Fracture traces obtained from field observations and Muldoon and Bradbury (1996). Well locations are shown as solid circles.

multi-azimuth line) using broadside antenna configuration A at 0°, 45°, 90°, and 135° to the azimuth of the survey line (Figure 7). Sixty-one CMPs were surveyed at 10 cm spacing, using 1.5-m antenna separation and 200-MHz center frequency. Fractures visible on the quarry floor were intersected by the survey line at normal and oblique angles.

Results

First we present the single midpoint multipolarization field data along with the analysis used to identify differences in the relative arrival times of the waveforms.

Single midpoint data.—Figure 8 displays GPR multipolarization data collected using varying antenna configurations at a single location on a fracture surface trace (Figures 8a–8e) and at a single location over the nonfractured quarry surface (Figures 8f–8g). The *H-pol* and *E-pol* time series displayed in Figure 8a were collected with a 0.5-m antenna offset using configuration A. For display purposes a [time]² gain factor is applied to the data. Visual inspection of the time series

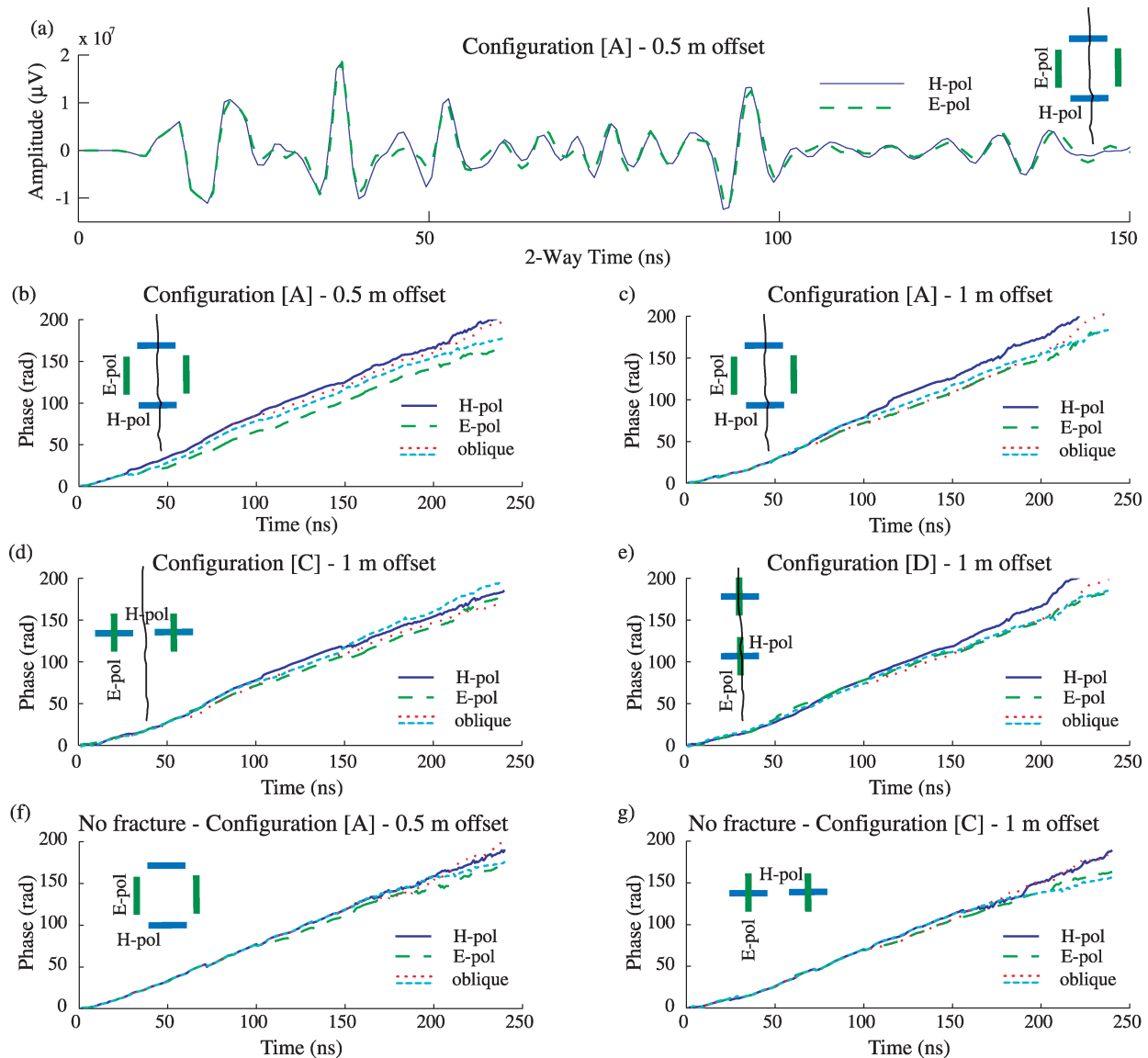


Figure 8. GPR multipolarization data collected at a single location on a fracture surface trace (a, b, c, d, e) and at a single location over a nonfractured quarry surface location (f, g). (a) Time series. (b–g) Complex trace phase angles. Refer to text for discussion.

(Figure 8a) indicates that *H*-pol leads in time *E*-pol at later times (80–140 ns), when greater angles of incidence to the vertical fracture plane would occur. A Δt of 0.15 ns (one-way time) is observed at the 95-ns reflector, and a Δt of 0.39 ns (one-way time) is observed at the 140-ns reflector. Both apparent time shifts are comparable to the time shifts observed in the modeled data of Figures 3 and 4. The differences in reflector arrival times between the two time series are evaluated by comparing the complex trace phase angles versus time for both polarizations (Figure 8b). The complex trace phase angle, also commonly referred to as instantaneous phase, is used to compare the relative arrival times of signals of similar form, as presented in Taner et al. (1979). The increasing separation between the phase curves shown in Figure 8b indicates increasing time separation between *H*-pol and *E*-pol as a function of increasing time (i.e., depth) or increasing angle of incidence to the vertical fracture plane. Also, *H*-pol is leading in phase compared to *E*-pol. The oblique polarization phase curves (45° , 135°) are expected to overlay each other based on numerical modeling simulations. However, a small phase separation is observed between oblique polarization data, probably because of dolomite matrix inhomogeneity and differences introduced by the varying travelpath azimuth.

A significant observation in the field data is the effect of antenna offset to the complex trace phase curves. Difference in phase for the 0.5-m offset configuration A data (Figure 8b) is observed at an earlier time (30 ns corresponding to $\theta_{if} \cong 80^\circ$) than the 1.0-m offset configuration A data (Figure 8c) (70 ns corresponding to $\theta_{if} \cong 82^\circ$) and at approximately the same angle of incidence (θ_{if}) to the plane of the fracture. The shorter offset data acquisition geometry results in high angles of incidence to the plane of the fracture at shallower depths and thus displays difference in phase earlier in time than the longer offset geometry.

Figures 8d and 8e display complex trace phase angles for multipolarization data collected using configurations C and D, with a 1-m offset. Again, *H*-pol is leading *E*-pol, and the oblique polarization phase curves show less separation. Note that antenna configurations C and D (Figures 8d and 8e) show reduced phase curve separation than configuration A (Figure 8c). We believe the optimum dipole antenna radiation pattern coupling between transmitter and receiver in the broadfire configuration A yields more consistent observations of the subsurface when compared to endfire configurations. Furthermore, data collected using configuration B showed significantly reduced phase separation and inconsistent phase relationship results, possibly from increased sensitivity of endfire geometry to accurate antenna alignment. Modeling indicates configuration B should also yield comparable phase separation data to the other configurations.

Figures 8f and 8g display complex trace phase angles for multipolarization data collected over the unfractured quarry surface using antenna configuration A at 0.5 m offset and configuration C at 1 m offset. Note that phase separation is minimal for the first 120 ns (compared to the first 30 and 70 ns of the fractured location). Antenna offset does not affect the onset of phase separation (compared to Figures 8b and 8d), and the difference in phase remains small for most of the record, comparable in magnitude to the oblique polarization data. Phase separation in the unfractured dolomite could be attributed to inhomogeneity in the rock matrix, small mispositioning of the

antennas, possible fracturing below surface, and low S/N ratio at later recording times.

Single-midpoint EM polarization data consistently show that when the electric field is oriented perpendicular to the plane of the fracture (*H*-pol), it leads in phase compared to an electric field oriented parallel to the fracture (*E*-pol), regardless of direction of propagation (across or along the fracture plane) or relative antenna geometry (broadfire or endfire). This observation allows for the prediction of location and azimuth of vertically oriented fractures.

Multipolarization 2D survey line.—Next, we test the applicability of our findings to a 2D multiazimuth survey line collected at Bissen Quarry. From the earlier analysis of the single-midpoint data and the fracture density shown in Figure 7 (drawn to scale), it becomes apparent that the 1.5-m antenna offset is too broad to measure the effects of single fractures and would limit the accuracy of individual vertical fracture detection. However, we proceed with the analysis, acknowledging potential limitations resulting from inappropriate survey geometry parameters.

Figure 9a displays the 0° azimuth, broadfire, along the survey line data, typically acquired with surface reflection GPR surveys. Because horizontal strata are not offset by vertical fractures, no evidence of the vertical fractures observed on the quarry floor (Figures 5 and 7) is detectable in any of the four azimuth data sets when examined individually. However, a simple subtraction of orthogonal polarization data 0° – 90° (Figure 9b) and 45° – 135° (Figure 9c) reveals phase and amplitude differences. Phase differences yield apparent amplitude variations that extend along the length of the trace, while

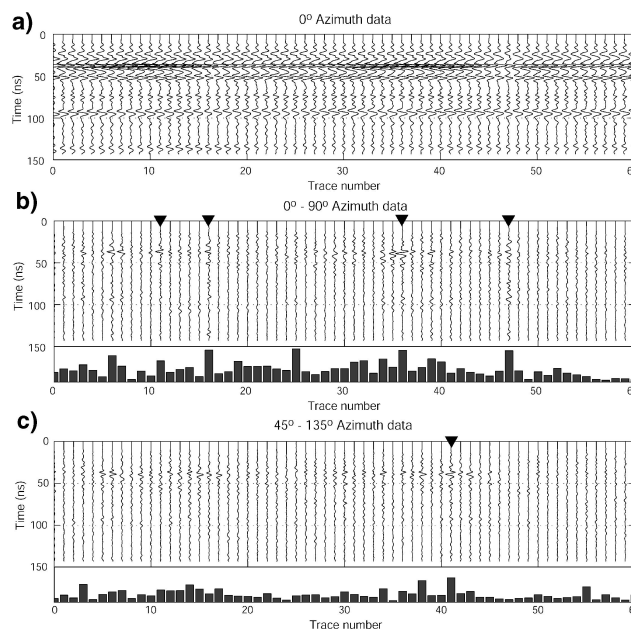


Figure 9. Multiazimuth 2D survey line data. (a) Broadfire along the survey line 0° azimuth data. (b) 0° – 90° azimuth data difference plot. (c) 45° – 135° azimuth data difference plot. The bar diagrams below (b) and (c) represent the sum of the squared amplitudes along each trace. Field observations of intersecting fracture traces are identified by solid triangles.

true amplitude differences attributable to dolomite inhomogeneity would have a localized or laterally extending expression. As expected, the smallest polarization differences are observed at the end of the line (CMP 50–60) where no fractures are present. Most of the polarization differences occur in two groups, coinciding with fracture density increase at CMPs 7–18 and 34–47 (Figures 7, 9b,c). Close inspection of the 0° – 90° profile (Figure 9b) shows significant trace differences at CMPs 11, 16, 36, and 47 where the survey line intersects fractures striking perpendicular to its direction. The 45° – 135° profile (Figure 9c) shows increased trace difference at CMPs 14–18 and 37–43 where the survey line intersects fractures at an oblique angle. Trace differences are also identified by the bar plots in Figures 9b,c, which represent the sum of the squared amplitudes along each trace. Because of the large antenna offset, multiple fracture effects are observed throughout the difference profiles. However, even with poor survey geometry, survey line intersections with fractures result in the strongest amplitude anomalies. Also, these amplitude anomalies appear to be dependent on the azimuth of the fractures, yielding different responses in the 0° – 90° and 45° – 135° profiles.

Complex trace phase angle analysis also supports the above observations. Figure 10 shows phase curves at locations where there is no fracture present (CMP 60), at an orthogonal fracture to the survey azimuth (CMP 47), at bifurcating oblique and orthogonal fractures (CMP 42), and at a fracture along the survey azimuth (CMP 14). Figure 10a, a nonfractured surface, shows overlaying complex trace phase curves and minimum phase curve separation. Figure 10b, an orthogonal fracture intersection, shows H -pol (90°) leading E -pol (0°) and small phase curve separation at the oblique polarizations (45° , 135°). Figure 10c, an oblique fracture intersection with an orthogonal bifurcation, shows H -pol (135°) leading E -pol (45°); while

the oblique polarizations (0° , 90°) show significant phase separation, and the 90° leads the 0° as expected for the orthogonal fracture bifurcation. Figure 10d, a fracture running along the survey line, shows a small phase lead of H -pol (0°) versus E -pol (90°).

These observations are consistent with earlier analyses of single midpoint field data, modeling, and analytic solutions. The 2D multi-azimuth data could not uniquely identify the location of each fracture because of the large antenna offset compared to fracture density. However, at the known midpoint locations where fractures intersected the survey line, $\Delta\phi$ is significant and the phase lead relationships are consistent with fracture orientations.

DISCUSSION AND CONCLUSIONS

Analytic computation of H -pol and E -pol transmission coefficients, 3D finite-difference time-domain simulations of EM wavefield propagation, and GPR field data demonstrate a consistent and detectable phase lead relationship between H -pol and E -pol waves, introduced by the high angle of incidence transmission through a vertical fracture. When the incident electric field is oriented perpendicular to the plane of the fracture (H -pol), the transmitted electric field leads in phase compared to when the incident electric field is parallel (E -pol) to the plane of the fracture. Thus, the location of a fracture can be identified based on the presence of a phase difference between orthogonal pairs of polarization data sets. Furthermore, the polarization trace leading in phase identifies the antenna axis azimuth orthogonal to the plane of the fracture, and the lagging polarization trace identifies the antenna axis azimuth parallel to the plane of the fracture. Thus, the azimuth of the fracture itself can be determined by the known antenna geometry relative to the survey line.

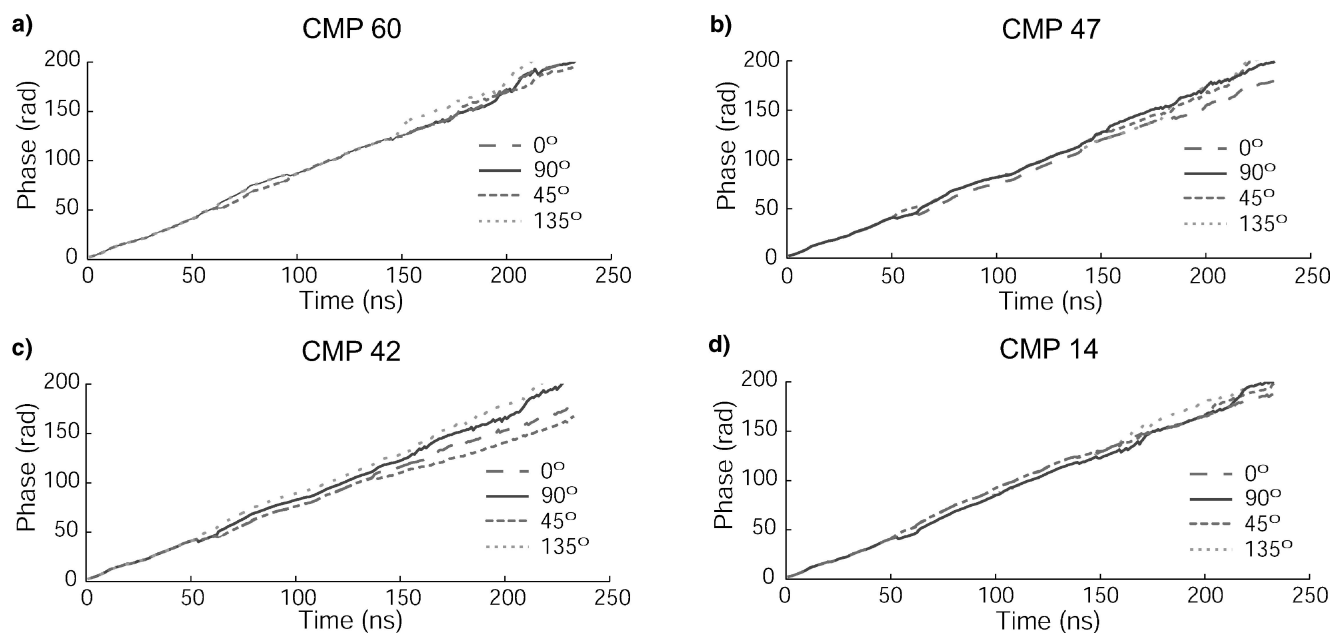


Figure 10. The 2D survey line multi-azimuth complex trace phase curves. (a) CMP 60, no fracture present. (b) CMP 47, orthogonal fracture to the survey azimuth. (c) CMP 42, bifurcating oblique and orthogonal fractures. (d) CMP 14, fracture along the survey azimuth.

Field data obtained using a commercially available GPR system with surface dipole antennas showed improved capability of vertical fracture detection when the relative antenna orientation was held in the broadside configuration (A), compared to endfire (B) and mixed (C, D) configurations. We believe this is the result of optimum coupling of the antenna radiation pattern between transmitter and receiver in the broadfire configuration. Constant wavefield azimuth configuration C could be used in areas of restricted surface survey area. Conceptually, configuration C could be applicable in wellbores for downhole fracture detection. For the proposed polarization surveying, antenna offset should be minimal to ensure high angles of incidence to vertical fracture planes and near-normal incidence to horizontal strata. Also, small antenna offset relative to fracture density would increase the potential of resolving individual fractures. In the case of dipping bedding planes, additional $\Delta\phi$ would be introduced by transmission and reflection through sloping interfaces. However, the sloping interface $\Delta\phi$ will be repeatable at each midpoint and, thus, discernible from $\Delta\phi$ introduced by the presence of a vertical fracture.

Finally, in polarization surveying for vertical fracture detection, caution should be used in accurately positioning the dipole antennas, both in offset and orientation, to detect reliably the vertical fracture-induced phase (apparent time) differences, which were shown in this study to be on the order of a fraction of a nanosecond (Figures 3b,c, 8a). Mispositioning antennas would result in travelpath variations between varying polarization recordings that would mask the $\Delta\phi$ introduced by the presence of a fracture. Use of an antenna platform that will allow consistently accurate positioning of the antennas will eliminate a potential source of uncertainty in phase-difference measurements. Furthermore, it will allow for quantitative interpretation of the phase-difference measurements and predict fracture aperture variation and fluid content changes, similar in concept to the comparison between the saturated and unsaturated fractured dolomite responses simulated in Figures 3c and 4.

Although field observations presented in this study are from a single site, the fractured Silurian Dolomite at Bissen Quarry, analytic computations and numerical simulations of varying geologic formations, varying fracture aperture and fluid content, and varying radar signal frequency support the methods presented and conclusions drawn in this study. Planned investigations will evaluate the feasibility of quantitative vertical fracture characterization using multipolarization GPR methods.

We conclude that multipolarization acquisition of GPR data offers the potential to detect the location and azimuth of thin, high-angle fractures in geologic formations. The data acquisition and analysis techniques presented in this study can be used to detect fractures beyond the resolution limitations of conventional copolarized reflection GPR data.

ACKNOWLEDGMENTS

The authors acknowledge the Geological Society of America, Gulf Coast Association of Geological Societies, and the Geology Foundation of the University of Texas at Austin for providing funds for the field work. We thank Jack Sharp, Matt

Peters, Sarah Tsoflias, and Todd Halihan for their input to this study. We also thank Ken Bradbury and Maureen Muldoon of the Wisconsin Geological and Natural History Survey for providing a wealth of supporting nonradar data about the field site and I. Bissen for allowing access to the field site. Also, we thank Roger Roberts for providing a copy of the 3D modeling code. Finally, we thank the reviewers of the manuscript for constructive comments and useful insights and suggestions for this work.

REFERENCES

- Alford, R. M., 1986, Shear data in the presence of azimuthal anisotropy: 56th Annual International Meeting, Society of Exploration Geophysicists, Expanded Abstracts, 476–479.
- Balanis, C., 1989, *Advanced Engineering Electromagnetics*: John Wiley & Sons, Inc.
- Birken, R., and Versteeg, R., 1998, Use of four dimensional GPR and advanced visualization methods to determine subsurface fluid flow: 7th International Conference on Ground Penetrating Radar, Proceedings, 1, 377–381.
- Brewster, M. L., and Annan, A. P., 1994, Ground-penetrating radar monitoring of a controlled DNAPL release: 200 MHz radar: *Geophysics*, **59**, 1211–1221.
- Chew, W. C., 1990, *Waves and fields in inhomogeneous media*: IEEE Press, Inc.
- Coon, J. B., Fowler, J. C., and Schafers, C. J., 1981, Experimental uses of short pulse radar in coal seams: *Geophysics*, **46**, 1163–1168.
- Davis, J. L., and Annan, A. P., 1989, Ground penetrating radar for high-resolution mapping of soil and rock stratigraphy: *Geophysical Prospecting*, **37**, 531–551.
- Fisher, E., McMechan, G. A., and Annan, A. P., 1992, Acquisition and processing of wide-aperture ground-penetrating radar data: *Geophysics*, **57**, 494–504.
- Grasmueck, M., 1996, 3-D ground-penetrating radar applied to fracture imaging in gneiss: *Geophysics*, **61**, 1050–1064.
- Kovacs, A., and Morey, R. M., 1978, Radar anisotropy of sea ice due to preferred azimuthal orientation of the horizontal *c* axes of ice crystals: *Journal of Geophysical Research*, **83**, 6037–6046.
- Lehmann, F., Boerner, D. E., Hollinger, K., and Green, A. G., 2000, Multicomponent georadar data: Some important implications for data acquisition and processing: *Geophysics*, **65**, 1542–1552.
- McMechan, G. A., Gaynor, G. C., and Szerbiak, R. B., 1997, Use of ground-penetrating radar for 3-D sedimentological characterization of clastic reservoir analogues: *Geophysics*, **62**, 786–796.
- Miwa, T., Sato, M., and Niitsuma, H., 1999, Subsurface fracture measurement with polarimetric borehole radar: *IEEE Transactions on Geosciences and Remote Sensing*, **37**, 828–837.
- Muldoon, M. A., and Bradbury, K. R., 1998, Hydrostratigraphy and tracer studies, Bissen Quarry: Conference on Fluid Flow in Carbonates, Interdisciplinary Approaches, Proceedings, 53–65.
- Muldoon, M. A., Simo, J. A., and Bradbury, K. R., 2001, Correlation of high permeability zones with stratigraphy in a fractured-dolomite aquifer, Door County, Wisconsin: *Hydrogeology Journal*, **9**, 570–583.
- Roberts, R. L., 1994, Analysis and theoretical modeling of GPR polarization phenomena: Ph.D. dissertation, The Ohio State University.
- Roberts, R. L., and Daniels, J. J., 1997, Modeling near-field GPR in three dimensions using the FDTD method: *Geophysics*, **62**, 1114–1126.
- Stratton, J. A., 1941, *Electromagnetic theory*: McGraw-Hill Book Company.
- Taner, M. T., Koehler, F., and Sheriff, R. E., 1979, Complex seismic trace analysis: *Geophysics*, **44**, 1041–1063.
- Tillard, S., 1994, Radar experiments in isotropic and anisotropic geological formations (granite and schists): *Geophysical Prospecting*, **42**, 615–636.
- Tsoflias, G. P., and Sharp, J. M., Jr., 1998, Three-dimensional hydrogeologic characterization of fractured carbonate aquifers using ground-penetrating radar: *Gulf Coast Association of Geological Societies Transactions*, **40**, 439–447.
- Tsoflias, G. P., Halihan, T., and Sharp, J. M., Jr., 2001, Monitoring pumping test response in a fractured aquifer using ground penetrating radar: *Water Resources Research*, **37**, 1221–1229.
- Van Gestel, J. P., and Stoffa, P. L., 2001, Application of Alford rotation to ground-penetrating radar data: *Geophysics*, **66**, 1781–1792.